

Identification and Control Design of a Sub-Scale Flybarless Helicopter

Jeffrey Walker
Bihrl Applied Research
Hampton, VA, USA

Mark B. Tischler
Tischler Aeronautics
Sunnyvale, CA, USA

ABSTRACT

This paper demonstrates the complete end-to-end procedure of bare-airframe system identification, Simulink control design, software-in-the-loop (SIL) validation, and flight testing for a sub-scale flybarless single main rotor configuration. Flight tests were conducted utilizing Pixhawk hardware in the form of a CUAVv5 flight computer running the ArduCopter software stack. CIFER[®] was utilized to process the flight data into the frequency domain and identify a higher-order hybrid model suitable for the highly-coupled rotor/fuselage dynamics of the sub-scale vehicle. An explicit model following control architecture was implemented to provide a stable hover controller utilizing MATLAB[®] and Simulink[®] control design tools. The controller was validated in the SIL environment using frequency domain techniques prior to conducting flight tests. Flight tests were used as a final demonstration of the designed control laws and uncovered sensor modeling deficiencies in the SIL environment.

NOTATION

ACAH attitude command attitude hold
 a_x longitudinal accelerometer body axis, [m/s²]
 a_y lateral accelerometer body axis, [m/s²]
 a_z vertical accelerometer body axis, [m/s²]
 CIFER[®] comprehensive identification from frequency response software
 CG center of gravity
 COTS commercial off the shelf
 CR Cramèr-Rao bound
 CZT chirp z-transform
 DRB disturbance rejection bandwidth, [rad/s]
 DRP disturbance rejection peak, [dB]
 e rotor-blade flapping hinge offset, [m]
 EKF extended Kalman filter
 EMF explicit model following
 f frequency, [Hz]
 FBW fly-by-wire
 g gravitational constant, [m/s²]
 GM gain margin, [dB]
 $\hat{\mathbf{G}}_{xx}, \hat{\mathbf{G}}_{xy}$ input and cross spectral density matrices
 $\hat{\mathbf{H}}(f)$ frequency response matrix
 $\mathbf{H}_0, \mathbf{H}_1$ state and state derivative measurement matrices
 h_r height of rotor hub above CG, [m]
 HIL hardware-in-the-loop
 IMU inertial measurement unit
 INS inertial navigation system
 I_{xx} roll moment of inertia, [kg-m²]
 I_{xz} product of inertia, [kg-m²]
 I_{yy} pitch moment of inertia, [kg-m²]

I_{zz} yaw moment of inertia, [kg-m²]
 J cost function for frequency response error
 K_β rotor-blade flap spring stiffness, [N-m/rad]
 L, M, N roll, pitch, yaw moments about CG, [N-m]
 $L_{\beta_{1s}}$ body roll moment due to tip path plane tilt, [1/s²]
 $L_{f\beta_{1s}}$ coupling term due to rotor flapping restraint, [1/s²]
 MEMS micro-electro-mechanical systems
 MIMO multi-input/multi-output
 $\mathbf{M}, \mathbf{F}, \mathbf{G}$ generalized equation of motion matrices of dynamical system
 M_β first mass moment of rotor blade, [kg-m]
 $M_{\beta_{1c}}$ body pitch moment due to tip path plane tilt, [1/s²]
 $M_{f\beta_{1c}}$ coupling term due to rotor flapping restraint, [1/s²]
 m_h vehicle mass, [kg]
 n_b number of blades
 PM phase margin, [deg]
 p angular roll rate, positive right wing down, [rad/s]
 q angular pitch rate, positive nose up, [rad/s]
 r angular yaw rate, positive nose right, [rad/s]
 R main rotor radius, [m]
 RC remote controlled
 SISO single-input/single-output
 s Laplace variable
 SIL software-in-the-loop
 U, V, W longitudinal, lateral, vertical total velocity components, [m/s]
 UAS unmanned aerial systems
 X, Y, Z longitudinal, lateral, vertical external forces on CG, [N]
 x_a IMU offset from CG, longitudinal body axis, [m]
 $X_{\beta_{1c}}$ longitudinal rotor force derivative, [m/s²]

y_a	IMU offset from CG, lateral body axis, [m]
$Y_{\beta_{1s}}$	lateral rotor force derivative, [m/s ²]
z_a	IMU offset from CG, vertical body axis, [m]
6DOF	six degree of freedom
β_{1c}	rotor longitudinal flapping angle, [rad]
β_{1s}	rotor lateral flapping angle, [rad]
δ_{lat}	roll control input
δ_{lon}	pitch control input
δ_{ped}	yaw control input
δ_{col}	vertical control input
γ^*	effective Lock number
γ_{xy}^2	coherence function between input x and output y
Ω	main rotor rotation speed, [rad/s]
ϕ	roll attitude, positive right wing down, [rad]
θ	pitch attitude, positive nose up, [rad]
ψ	yaw attitude, positive nose right, [rad]
τ	time delay, [sec]
τ_f	rotor flap time constant, [sec]
τ_p	phase delay, [sec]
λ	eigenvalue
ω_n	natural frequency, [rad/s]
ζ	damping ratio

Subscripts

0	trim value
BL	broken-loop
BW	bandwidth
c	crossover
cm	command model
d	disturbance
e	error
fb	feedback
ff	feed-forward
I	imaginary part
n	natural frequency
R	real part

INTRODUCTION

Small unmanned aerial systems (UAS) have become prevalent in recent years thanks to the advancements and affordability of small electronics and the ongoing open-source development of the software that many of these vehicles leverage (e.g., Pixhawk, ArduCopter). These small UAS have a wide range of uses including, but not limited to, hobbyist flying, linear infrastructure inspection, package delivery, search and rescue, and military intelligence surveillance reconnaissance applications. As these vehicles become more familiar and readily available, it can be tempting to empirically adjust gains to get a vehicle in the air quickly, overlooking the value of methodical flight control development techniques using system identification and classical control methods. As with full-scale aircraft, empirical gain tuning will not provide for most efficient use of the available control authority, nor

allow a systematic investigation of the control design trade-offs (Ref. 1), which is especially important as UAS begin to operate closer to populated areas and perform more demanding tasks.

Rotorcraft system identification is a field that has seen many applications with various vehicles from full to small sized helicopters and multi-rotor configurations and plays a key role in the control system design and validation process (Refs. 2, 3). Excellent tools such as CIPHER[®] (Ref. 2) exist for engineers to perform system identification; however, it is very much a learned process that requires an understanding of the underlying dynamics. Aside from full scale vehicles, most past UAS rotorcraft system identification has focused on larger flybar equipped vehicles such as the Yamaha R-50 (Ref. 4) and Raptor (Ref. 5) and more recently multi-rotor vehicles (Refs. 3, 6) have been a focus, in part, due to their mechanical simplicity.

Early research efforts such as (Refs. 4, 5) used mechanical flybar equipped helicopters as this was the common configuration used by recreational pilots at the time. The flybar provides lagged rate feedback that helps stabilize the aircraft and has the overall effect of slowing the response time of the aircraft to control inputs, as shown later in this paper, thereby improving piloted handling-qualities. These efforts played a significant role investigating the effects the stabilizer bar has on rotor dynamics as well as the importance of dynamic scaling of small vehicles. However, modern MEMS electronics have resulted in flybarless helicopters as the common configuration among recreational pilots who utilize three axis gyro stabilization systems to allow for manual flight of vehicles that would otherwise be unstable. These systems have enabled recent research using smaller more maneuverable helicopter configurations.

Alvarenga (Refs. 7, 8) used CIPHER[®] to identify a vehicle model for the DU²SRI Bergen Industrial Turbine helicopter that utilizes a flybarless configuration. The Bergen aircraft is considerably larger with a rotor diameter twice the size of the vehicle utilized in the present research. Also, the model formulation included identification parameters of the feedback elements in addition to the bare-airframe which resulted in large Cramèr-Rao bounds and insensitivities in key parameters.

Reference 9 compared the maneuverability of flybar and flybarless micro-scale helicopters and noted that the flybarless configuration had an unstable mode, highly-coupled dynamics and greater maneuverability than the equivalently scaled flybar counterpart. Taamallah (Refs. 10, 11) investigated flight dynamics modeling specific to the configuration of remote controlled flybarless helicopters utilizing first principles modeling and compared results to a FLIGHTLAB simulation. Zhou (Ref. 12) presented a nonlinear system identification method in the time domain used to model a small-scale flybarless helicopter of similar size to the vehicle used by Alvarenga.

The primary contribution of this effort is the end-to-end application of the full-scale flight control development process to sub-scale flybarless helicopter for a hover/low-speed flight

condition. The work starts with the CIFER[®] identification of a sub-scale flybarless helicopter, and compares the dynamics characteristics with those of prior commonly used fly-bar type configurations. Next, based on this accurate model of the bare-airframe, a flight control system design is completed for an explicit model-following (EMF) flight control architecture, commonly used for full-scale fly-by-wire (FBW) rotorcraft. Special aspects of the EMF implementation are due to the highly-coupled fuselage/flap response. Then, software-in-the-loop (SIL) simulations were used to integrate the real-time control laws in the actual flight computer and validate the flight control response characteristics with the design models. Finally, flight testing was conducted to validate the control system performance based on comparison with the SIL and design model. Thus, this study presents the complete end-to-end process from system identification to control law synthesis, simulation validation, and flight testing.

FLIGHT VEHICLE

The sub-scale helicopter utilized by this study is the Blade 360CFX 3S manufactured by Horizon Hobby (Figure 1). The 360CFX has a main rotor diameter of 0.8m and an approximate mass of 0.68 kg in the COTS configuration. The vehicle was equipped with an additional sensor payload including a CUAUV5 flight computer (replacing the COTS stabilization system) which increased the empty mass to 0.985 kg. The additional sensor payload added more mass below the center of gravity compared to the COTS configuration which resulted in more docile flight characteristics. Table 1 presents further vehicle properties including inertia values that were estimated using the bifilar pendulum method as described by (Refs. 13, 14).

The 360CFX utilizes a flybarless rotor head configuration which is the common configuration among modern RC helicopters. The mechanical actuation of the main rotor head consists of pitch at the rotor hub, lead-lag from a damper at the blade connection bolt, and flapping through the flexibility of the carbon blades. Equations of motion for this particular hinge arrangement have been derived in (Refs. 10, 11). Unlike flybar equipped vehicles, the flybarless configuration require a three-axis attitude and rate feedback system to stabilize the vehicle for piloted operations. This is a result of the rigid rotor head that produces larger moments and lack of a flybar to damp the fast dynamic response.

Table 1. Vehicle Properties

Property	Value	Units
m_h (with battery)	1.4055	kg
I_{xx}	0.0583	kg – m ²
I_{yy}	0.0377	kg – m ²
I_{zz}	0.0835	kg – m ²
I_{xz}	5.55E-4	kg – m ²
Main Rotor Diameter	0.8128	m
Main Rotor Rotation Speed	230	rad/s



Figure 1. Blade 360-CFX 3S Helicopter

The open source ArduCopter software package was utilized onboard the CUAUV5 flight computer (Ref. 15). The ArduCopter software provides support for traditional helicopter configurations and has the back-end infrastructure to conduct SIL and HIL testing. Additionally, the ability to obtain direct measurements of the control system commands from within ArduCopter facilitates the identification of the bare-airframe dynamics model. The initial flight tests were conducted utilizing a development branch from version 3.6 of the software that had been configured for automated sweep testing (Ref. 16) and used empirically tuned gains. Subsequent control development work utilized version 4.1 of the software as it added a SIL interface that enabled hosting the vehicle flight dynamics within Simulink[®].

SYSTEM IDENTIFICATION

System identification was carried out using the frequency-response identification method and the Comprehensive Identification from Frequency Responses (CIFER[®]) software package (Ref. 2). This system identification method and software is described in detail by (Ref. 2). Only a brief outline of the method will be given herein. The identification process is comprised of three major steps: 1) Identification of the multi-input/multi-output (MIMO) frequency response matrix from flight-test data; 2) Development and identification of a parametric state-space stability and control derivative model that best matches the MIMO frequency response matrix; and, 3) Verification of the resulting state-space model with flight-data time responses not used in the identification process.

The first step is accomplished with flight-test data using manual or automated inputs that adequately excite the helicopter over the frequency range of interest. For flybarless UAS, a simple ArduCopter “Stabilize” (or “Acro”) controller allows the identification tests to be conducted with automated inputs and small piloted corrections. Ideally for this identification approach, the input is a “frequency sweep” with a frequency progression from low to high frequency, covering the frequency range of concern for the vehicle (1-100 rad/sec in this case). The input and vehicle response starts and ends in trim. A fast Fourier transform, using the chirp z-transform (CZT), and composite window averaging converts the data from the time- to frequency- domain. Then the MIMO frequency-

response matrix is determined from the input spectral density and cross-spectral-density matrices (Ref. 2):

$$\hat{\mathbf{H}}(f) = \hat{\mathbf{G}}_{xx}^{-1}(f)\hat{\mathbf{G}}_{xy}(f) \quad (1)$$

This MIMO frequency-response matrix solution yields the correct single-input/single-output (SISO) frequency responses when multiple control inputs are present and partially correlated in the test data, which is usually the case for helicopter tests. For single input tests, Equation 1 reduces to the more familiar scalar relationship. A key indicator of the accuracy of each resulting frequency response is the associated coherence function $\hat{\gamma}_{xy}^2(f)$ which is also determined from the spectral density functions (Ref. 2). A coherence value nearing unity indicates a high signal-to-noise ratio of the flight-test data and a highly-accurate frequency response. High coherence is achieved using frequency-sweep inputs, owing to their rich spectral content, and persistent excitation throughout the flight maneuver.

After the frequency responses are calculated, the second step is to hypothesize a state-space stability-derivative model:

$$\begin{aligned} \mathbf{M}\dot{\mathbf{x}} &= \mathbf{F}\mathbf{x} + \mathbf{G}u(t - \tau) \\ \mathbf{y} &= \mathbf{H}_0\mathbf{x} + \mathbf{H}_1\dot{\mathbf{x}} \end{aligned} \quad (2)$$

based on a physical understanding of the vehicle's primary flight dynamics. An optimization scheme employing a secant search then determines the free model parameters by minimizing the error in both magnitude and phase between the model and flight-test responses. The accuracy of the identified model is judged from the overall frequency-domain cost function J_{ave} , where $J_{ave} \leq 100$ reflects an acceptable level of accuracy and $J_{ave} \leq 50$ reflects an identified model that is nearly indistinguishable from the flight data.

Confidence analyses are performed on the converged model by determining the Hessian matrix and resulting theoretical accuracy metrics: Cramér-Rao bounds ($\overline{CR}_i, \%$) and Insensitivities ($\overline{I}_i, \%$). Identified parameters that are insensitive ($\overline{I}_i > 10\%$) or highly correlated ($\overline{CR}_i > 20\%$) are sequentially eliminated or fixed to a reliable a priori value, reducing the model complexity, and the optimization scheme is repeated.

The final step, after a satisfactory model has been identified, is to drive the model with flight-test doublet inputs (which were not used in the identification process) for comparison with flight-test responses. This final step verifies both the final model structure and its identified values.

Flight Test

Flight tests were conducted in calm conditions to minimize the influence of external disturbances and reduce the required pilot inputs to maintain the hover condition. Throughout flight testing the vehicle was flown using ACRO mode which provides rate command attitude hold control of the vehicle. This mode was chosen over the STABILIZE flight mode as it allowed the vehicle to more freely respond to the sweep inputs

in contrast to STABILIZE mode which attempts to hold zero roll and pitch attitude in the absence of pilot inputs.

Data was logged at the highest available rate of 400Hz and all signals were filtered onboard using a 100Hz low-pass filter. Significant signals of interest for identification purposes consisted of the translational accelerations a_x, a_y, a_z , angular rates p, q, r , angular attitudes ϕ, θ, ψ , and control inputs $\delta_{lat}, \delta_{lon}, \delta_{ped}, \delta_{cot}$. The control input signals were pulled before the mixer to ensure identification of the bare-airframe in pilot stick axes as depicted in Figure 9. The accelerations and angular rates sourced from the INS and the attitude signals from the EKF solution.

Preliminary flight tests were conducted using manual sweeps, orthogonal multisines, and automated sweeps. Automated sweeps implemented as described by (Ref. 2) provided the best coherence and were ultimately utilized. Automated doublets were performed to collect dissimilar data for model validation purposes. Figure 2 depicts an example automated sweep signal (δ_{latBL}), the total lateral control output (δ_{lat}), and the resultant roll rate response.

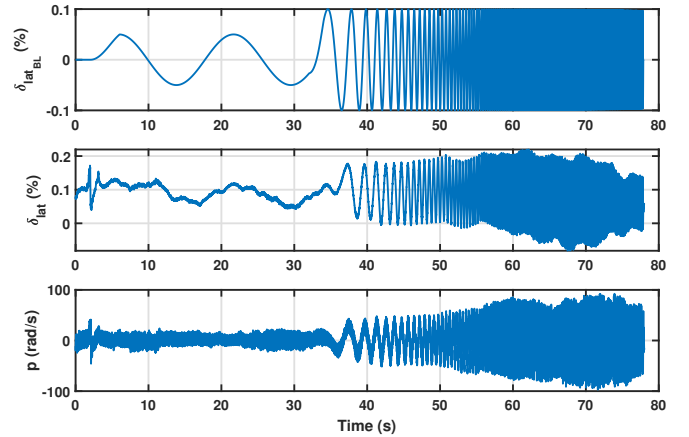


Figure 2. Example Automated Lateral Sweep

Collecting data with good coherence at low frequencies is especially difficult for small vehicles which compromises the accuracy of identified speed-stability derivatives (L_v, M_u, N_v). To overcome this obstacle, it is common to utilize speed trim data (Ref. 2). To facilitate this testing a velocity controller was implemented that allowed the pilot to command body axis longitudinal and lateral velocities at four velocity detents while holding altitude. This data was then utilized to determine the trim control gradients, $\Delta\delta_{lon}/\Delta u, \Delta\delta_{lat}/\Delta v, \Delta\delta_{ped}/\Delta v$ which were utilized in Equations 3 to 5 to fix the derivatives in the model.

$$L_v = - \left[L_{\delta_{lat}} \left(\frac{\Delta \delta_{lat}}{\Delta v} \right) + L_{\delta_{ped}} \left(\frac{\Delta \delta_{ped}}{\Delta v} \right) \right] \quad (3)$$

$$M_u = -M_{\delta_{lon}} \left(\frac{\Delta \delta_{lon}}{\Delta u} \right) + M_w \frac{Z_u}{Z_w} \quad (4)$$

$$N_v = -N_{\delta_{ped}} \left(\frac{\Delta \delta_{ped}}{\Delta v} \right) \quad (5)$$

Data Processing

Post flight data was processed using MATLAB and a custom suite of software wrapped around ArduPilot (Ref. 17) which greatly simplified the extraction of relevant signals from ArduCopter data logs for use within CIPHER[®]. The angular kinematic consistency was checked within CIPHER[®] using NAVFIT to identify a scale factor and time delay using the formulation presented in Equation 6 for the roll axis. Figure 3 depicts an example of the inconsistency between roll rate and roll attitude where it is observed that ϕ leads p by approximately 14 milliseconds. The lead is attributed to the onboard filtering of the INS rate gyro signals. Synchronization corrections were implemented by shifting the attitude signals and then interpolating the data to obtain the required time samples.

$$\frac{\phi}{p} s = K e^{-\tau s} \quad (6)$$

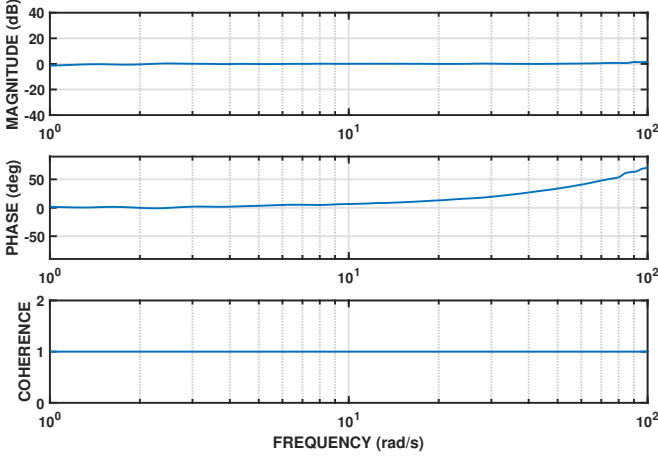


Figure 3. $\frac{\phi}{p}$ s Indicating Kinematic Inconsistency

The required body axis accelerations at the IMU location were reconstructed using Equations 7 to 9. This approach is easily accomplished in FRESPIID and avoids using the highly processed EKF signals thereby providing higher coherence and overall improved data quality (Ref. 2).

$$\dot{u}_{IMU} = a_{x_{IMU}} - W_0 q + V_0 r - (g \cos \theta_0) \theta \quad (7)$$

$$\dot{v}_{IMU} = a_{y_{IMU}} - U_0 r + W_0 p + (g \cos \theta_0) \phi - z_a \dot{p} + x_a \dot{r} \quad (8)$$

$$\dot{w}_{IMU} = a_{z_{IMU}} - V_0 p + U_0 q + (g \sin \theta_0) \theta + y_a \dot{p} - x_a \dot{q} \quad (9)$$

Multiple flight events from each axis were combined using the combination of FRESPIID, MISOSA, and COMPOSITE tools within CIPHER[®]. This provided frequency response data with high coherence over a broad frequency range as depicted in Table 2. The nearly equivalent range of acceptable coherence in the on- and off- axis responses for both the lateral and longitudinal axes indicate the vehicle exhibits a strong level of coupling.

Table 2. Frequency Response Pairs (rad/s)

	δ_{lat}	δ_{lon}	δ_{ped}	δ_{col}
a_x	[11.6 99.0]	[1.7 101.0]	-	-
a_y	[1.4 110.0]	[10.0 60.0]	-	-
a_z	-	-	-	[0.6 90]
\dot{u}	[11.6 99.0]	[1.7 101.0]	-	-
\dot{v}	[1.4 110.0]	[10.0 60.0]	-	-
\dot{w}	-	-	-	[0.6 90]
p	[1.4 110.0]	[10.0 60.0]	-	-
q	[11.6 99.0]	[1.7 101.0]	-	-
r	-	-	[3.0 134.0]	[3.0 6.7]

In order to identify a model that represents the vehicle at the CG it is necessary to appropriately account for the IMU offsets (x_a, y_a, z_a) in the measurement matrices. The velocity responses are accounted for by including Equation 10 and similarly the accelerometer responses with Equation 11. Equations 10 and 11 are implemented in the measurement equation (Equation 2) using the \mathbf{H}_0 and \mathbf{H}_1 matrices.

$$\begin{aligned} u_{IMU} &= u_{CG} + z_a q - y_a r \\ v_{IMU} &= v_{CG} - z_a p + x_a r \\ w_{IMU} &= w_{CG} + y_a p - x_a q \end{aligned} \quad (10)$$

$$\begin{aligned} a_{x_{IMU}} &= \dot{u} + W_0 q - V_0 r + (g \cos \theta_0) \theta + z_a \dot{q} - y_a \dot{r} \\ a_{y_{IMU}} &= \dot{v} + U_0 r - W_0 p - (g \cos \theta_0) \phi - z_a \dot{p} + x_a \dot{r} \\ a_{z_{IMU}} &= \dot{w} + V_0 p - U_0 q + (g \sin \theta_0) \theta + y_a \dot{p} - x_a \dot{q} \end{aligned} \quad (11)$$

State-Space Model Identification: 6DOF Model

A quasi-steady 6DOF model was initially identified over the limited range of 2 – 25 rad/s. The model adequately captured the first order yaw and heave dynamics. However, the lateral and longitudinal rotor-fuselage coupling cannot be accurately modeled using the 6DOF framework as depicted in Figure 4. This limitation of the 6DOF model is expected as the required lightly coupled condition of Equation 12 (Ref. 2) does not hold true for the 360CFX.

$$\tau_f^2 \ll \left| \frac{1}{L_{\beta_{1s}}} \right| \quad (12)$$

Thus, the coupled high-order rotor/fuselage or “hybrid model” as presented by Reference 2 is required to accurately model the vehicle dynamics for the purpose of control design.

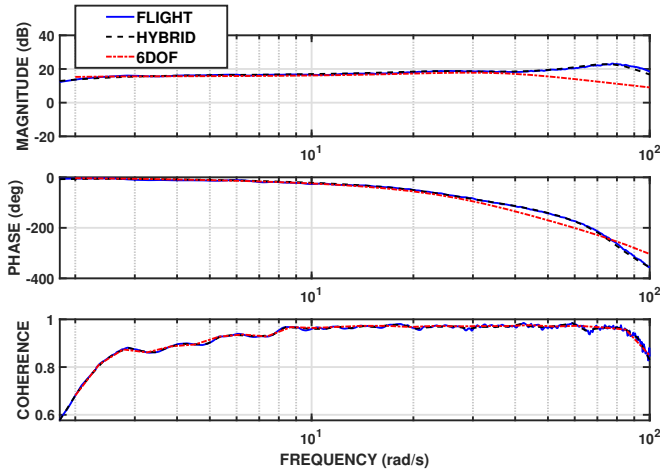


Figure 4. Quasi-Steady 6DOF p/δ_{lat}

State-Space Model Identification: Hybrid Model

The hybrid model formulation extends the 6DOF model to explicitly include the coupled fuselage/rotor flapping dynamics (Ref. 2). This allows the hybrid model to accurately capture the second-order regressive flapping mode as demonstrated in Figure 4. The simplified first order flapping dynamics included in the hybrid formulation are presented in Equation 13 (Ref. 2).

$$\begin{aligned}\tau_f \dot{\beta}_{1c} &= -\beta_{1c} + Mf_{\beta_{1s}} \beta_{1s} + \tau_f q + Mf_{\delta_{lon}} \delta_{lon} + Mf_{\delta_{lat}} \delta_{lat} \\ \tau_f \dot{\beta}_{1s} &= -\beta_{1s} + Lf_{\beta_{1c}} \beta_{1c} + \tau_f p + Lf_{\delta_{lon}} \delta_{lon} + Lf_{\delta_{lat}} \delta_{lat}\end{aligned}\quad (13)$$

The hybrid model outputs, states, and inputs are defined by Equation 14 and the detailed matrix equations that constitute the identified hybrid model are presented in Equations 15 to 19. The rotor flap time constant is included in the \mathbf{M} matrix as presented in Equation 15. Equation 16 presents the system dynamics matrix where the hover trim attitudes $\phi_0 = 3.4$ (deg), $\theta_0 = -0.3$ (deg) have been omitted for brevity. The control input matrix is presented in Equation 17 and the measurement matrices that account for the IMU offset are presented in Equations 18 and 19.

$$\begin{aligned}y &= [u \ v \ w \ p \ q \ r \ a_x \ a_y \ a_z \ \phi \ \theta]^T \\ x &= [u \ v \ w \ p \ q \ r \ \phi \ \theta \ \beta_{1c} \ \beta_{1s}]^T \\ u &= [\delta_{lat} \ \delta_{lon} \ \delta_{ped} \ \delta_{col}]^T\end{aligned}\quad (14)$$

$$\mathbf{M} = \begin{bmatrix} I_{8 \times 8} & 0_{8 \times 1} & 0_{8 \times 1} \\ 0_{1 \times 8} & \tau_f & 0 \\ 0_{1 \times 8} & 0 & \tau_f \end{bmatrix}\quad (15)$$

$$\mathbf{F} = \begin{bmatrix} X_u & X_v & 0 & 0 & 0 & 0 & 0 & -g & X_{\beta_{1c}} & 0 \\ Y_u & Y_v & 0 & Y_p & 0 & 0 & g & 0 & 0 & Y_{\beta_{1s}} \\ 0 & 0 & Z_w & 0 & 0 & 0 & 0 & 0 & 0 & 0 \\ L_u & L_v & 0 & 0 & 0 & 0 & 0 & 0 & 0 & L_{\beta_{1s}} \\ M_u & M_v & 0 & 0 & 0 & 0 & 0 & 0 & M_{\beta_{1c}} & 0 \\ 0 & N_v & N_w & 0 & 0 & N_r & 0 & 0 & 0 & 0 \\ 0 & 0 & 0 & 1 & 0 & 0 & 0 & 0 & 0 & 0 \\ 0 & 0 & 0 & 0 & 1 & 0 & 0 & 0 & 0 & 0 \\ 0 & 0 & 0 & 0 & \tau_f & 0 & 0 & 0 & -1 & Mf_{\beta_{1s}} \\ 0 & 0 & 0 & \tau_f & 0 & 0 & 0 & 0 & Lf_{\beta_{1c}} & -1 \end{bmatrix}\quad (16)$$

$$\mathbf{G} = \begin{bmatrix} 0 & 0 & 0 & 0 \\ 0 & 0 & 0 & 0 \\ 0 & 0 & 0 & Z_{\delta_{col}} \\ 0 & 0 & 0 & 0 \\ 0 & 0 & N_{\delta_{ped}} & N_{\delta_{col}} \\ 0 & 0 & 0 & 0 \\ 0 & 0 & 0 & 0 \\ Mf_{\delta_{lat}} & Mf_{\delta_{lon}} & 0 & 0 \\ Lf_{\delta_{lat}} & Lf_{\delta_{lon}} & 0 & 0 \end{bmatrix}\quad (17)$$

$$\mathbf{H}_0 = \begin{bmatrix} 1 & 0 & 0 & 0 & z_a & -y_a & 0 & 0 & 0 & 0 \\ 0 & 1 & 0 & -z_a & 0 & x_a & 0 & 0 & 0 & 0 \\ 0 & 0 & 1 & y_a & -x_a & 0 & 0 & 0 & 0 & 0 \\ 0 & 0 & 0 & 1 & 0 & 0 & 0 & 0 & 0 & 0 \\ 0 & 0 & 0 & 0 & 1 & 0 & 0 & 0 & 0 & 0 \\ 0 & 0 & 0 & 0 & 0 & 1 & 0 & 0 & 0 & 0 \\ 0 & 0 & 0 & 0 & 0 & 0 & 0 & g & 0 & 0 \\ 0 & 0 & 0 & 0 & 0 & 0 & -g & 0 & 0 & 0 \\ 0 & 0 & 0 & 0 & 0 & 0 & 0 & 0 & 0 & 0 \\ 0 & 0 & 0 & 0 & 0 & 0 & 1 & 0 & 0 & 0 \\ 0 & 0 & 0 & 0 & 0 & 0 & 0 & 1 & 0 & 0 \end{bmatrix}\quad (18)$$

$$\mathbf{H}_1 = \begin{bmatrix} 0_{6 \times 1} & 0_{6 \times 4} \\ 1 & 0 & 0 & 0 & z_a & -y_a & 0_{1 \times 4} \\ 0 & 1 & 0 & -z_a & 0 & x_a & 0_{1 \times 4} \\ 0 & 0 & 1 & y_a & -x_a & 0 & 0_{1 \times 4} \\ 0_{2 \times 1} & 0_{2 \times 4} \end{bmatrix}\quad (19)$$

Identification of the hybrid model was conducted using DE-RIVID with initial model parameters set to the identified 6DOF values wherever possible. The rotor time constant was initially estimated using Equation 20 and the rotor-fuselage coupling terms were estimated using Equations 21 and 22 (Ref. 2). The theoretical value of g was used for $X_{\beta_{1c}}$ and the physical constraint $Y_{\beta_{1s}} = -X_{\beta_{1c}}$ was imposed.

$$\frac{1}{\tau_f} = \frac{\gamma^* \Omega}{16} \left(1 - \frac{8e}{3R} \right)\quad (20)$$

$$-L_{\beta_{1s}} = \frac{m_h h_r}{I_{xx}} + \frac{n_b M_\beta \Omega^2 e}{2I_{xx}} + \frac{n_b K_\beta}{2I_{xx}} \quad (21)$$

$$-M_{\beta_{1c}} = \frac{m_h h_r}{I_{yy}} + \frac{n_b M_\beta \Omega^2 e}{2I_{yy}} + \frac{n_b K_\beta}{2I_{yy}} \quad (22)$$

The model reduction process summarized above and covered in detail by (Ref. 2) was followed, providing a systematic process to arrive at the final model structure and physical insight into the important vehicle parameters. Figures 5 and 6 present the primary on-axis frequency responses for the final identified model for the lateral and longitudinal axes and show the prominent coupled rotor-fuselage mode. The eigenvalues and corresponding modes of the identified model are tabulated in Table 3, and also indicate the presence of strong rotor-fuselage coupling as no distinct lateral/longitudinal quasi-steady fuselage modes exist. This strong coupling is a result of the small vehicle size and is in agreement with the Froude dynamic scaling laws that indicate flap stiffness will increase with the scale factor N thereby necessitating the use of the hybrid formulation (Ref. 2).

Table 3. Hybrid Model Eigenvalues

	$(\lambda_i)_R$	$(\lambda_i)_I$	ζ	ω (rad/s)	Mode
λ_1	-0.59	0.00	-	-	DIR/HEAVE
λ_2	0.94	0.80	-0.76	1.24	DIR/HEAVE
λ_3	0.94	-0.80	-0.76	1.24	DIR/HEAVE
λ_4	-1.22	-0.71	0.87	1.41	DIR/LAT
λ_5	-1.22	0.71	0.87	1.41	DIR/LAT
λ_6	-2.02	0.00	-	-	DIR
λ_7	-11.83	-22.97	0.46	25.84	LON/FLAP
λ_8	-11.83	22.97	0.46	25.84	LON/FLAP
λ_9	-16.38	-76.41	0.21	78.15	LAT/FLAP
λ_{10}	-16.38	76.41	0.21	78.15	LAT/FLAP

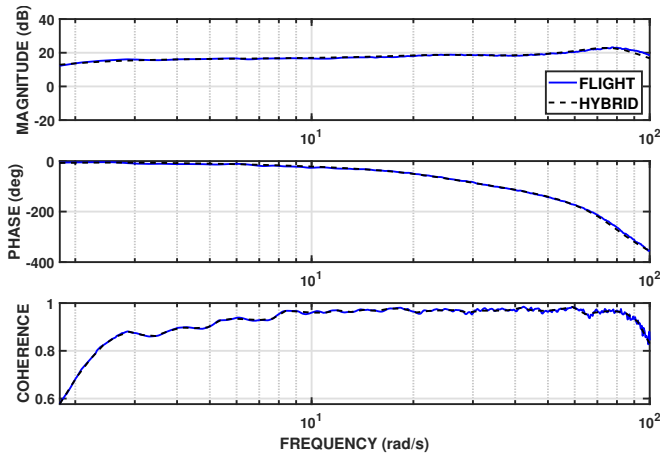


Figure 5. Hybrid p/δ_{lat}

Utilization of the explicit flapping equations in the hybrid model provided excellent agreement with the flight test data as

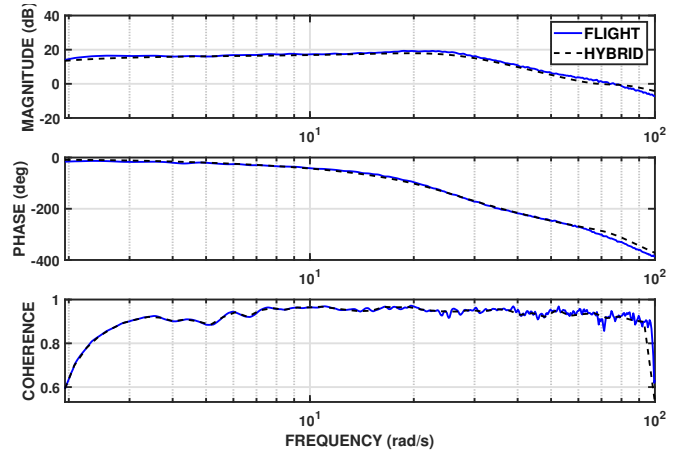


Figure 6. Hybrid q/δ_{lon}

indicated by Table 4 and the low average cost function value $J_{ave} = 58$ indicating an excellent model of the flight dynamics. This agreement was validated in the time domain using the automated doublet data and is presented in Figure 7 for a lateral control doublet and Figure 8 for a longitudinal doublet that demonstrates the strong coupling between the two axes. The final identified model parameters and their respective Cramèr-Rao bounds and insensitivities are presented in Table 5.

Table 4. Hybrid Model and Average Cost

Response	Costs
u/δ_{lat}	112.9
v/δ_{lat}	10.1
p/δ_{lat}	10.2
q/δ_{lat}	118.1
a_x/δ_{lat}	112.6
a_y/δ_{lat}	15.9
u/δ_{lon}	64.8
v/δ_{lon}	47.3
p/δ_{lon}	78.9
q/δ_{lon}	35.1
a_x/δ_{lon}	101.6
a_y/δ_{lon}	47.8
r/δ_{ped}	61.7
w/δ_{col}	22.9
r/δ_{col}	65.4
a_z/δ_{col}	23.2
J_{ave}	58.0

In (Ref. 2) the R-50 rotor flap stiffness was compared to the Honeybee (Ref. 18) which is a small flybar equipped helicopter. Table 6 utilizes the R-50 vehicle as the reference model and demonstrates that as the scale of the vehicle gets smaller, the roll flap stiffness increases, which is consistent with the Froude scaling properties, but *drastically more so for flybarless vehicles*. This is especially apparent in the comparison of the 360CFX (flybarless) and Raptor (flybar) vehicles that are very close in scale.

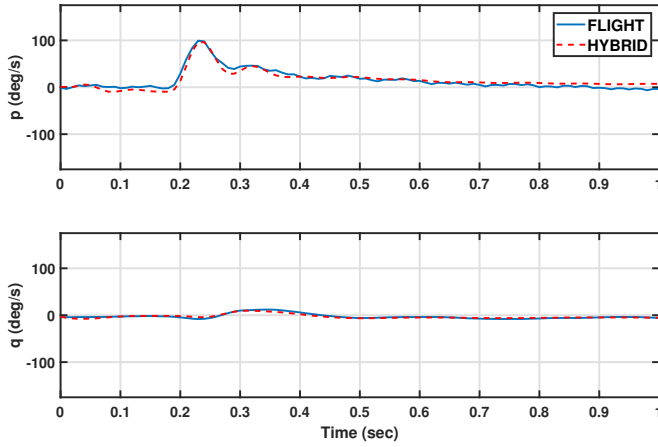


Figure 7. Hybrid Roll and Pitch Rate Response to Lateral Doublet

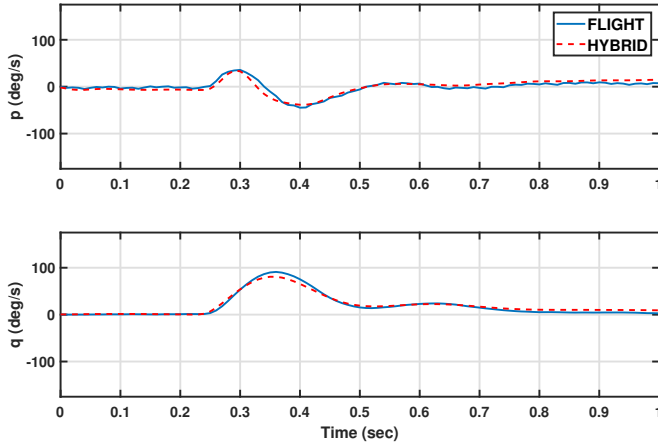


Figure 8. Hybrid Roll and Pitch Rate Response to Longitudinal Doublet

A parameter that is useful to characterize the vehicle response is the overall angular response time constant, $\tau_{eff} = 2\zeta/\omega_n$ (Ref. 2), where $\omega_n = \sqrt{-(L\beta_{1s})}$; $2\zeta\omega_n = 1/\tau_f$. So, $\zeta = (1/\tau_f)/(2\omega_n)$. For the 360CFX (flybarless) helicopter, using values from Table 5, the roll natural frequency is computed as $\omega_n = 71.52\text{rad/s}$ and the damping $\zeta = 0.198$ resulting in the overall time constant $(\tau_{eff})_{CFX} = 0.0055\text{sec}$. For the Raptor, which is the same vehicle size (N): $(\tau_{eff})_{RAPTOR} = 0.43\text{sec}$ is much larger than CFX due to the effect of the flybar. This shows dramatic effect of the flybar on the vehicle angular response time constant.

ACAH CONTROL DESIGN

Once an accurate model has been identified, the control design task can be executed. The intent of the controller presented in this study is to provide a stable hover response in order to demonstrate the design procedure. Thus, the design presented herein does not reflect an optimized design nor does it account for the extensive number of control objectives that are typically considered.

Table 5. Identified Parameters for Hybrid Model

Parameter	Value	CR, %	Insens, %
X_u	-0.2270	15.219	6.4927
$X_{\beta_{1c}}$	-9.81 ^a	-	-
Y_v	-0.1852 ^b	-	-
Y_p	0.2303	15.103	6.7390
$Y_{\beta_{1s}}$	$-X_{\beta_{1c}}$	-	-
Z_w	-0.5910	13.934	6.5631
L_u	-28.7796	30.183	9.8609
L_v	-5.5376 ^b	-	-
$L_{\beta_{1s}}$	-5115.2461	2.579	0.7706
M_u	2.7501 ^b	-	-
M_v	-2.3039	28.816	11.4522
$M_{\beta_{1c}}$	-796.7114	2.884	0.7188
N_v	1.7258 ^b	-	-
N_w	5.7574	14.921	3.8510
N_r	-2.0131	18.803	5.0135
$Mf_{\beta_{1s}}$	-1.0057	4.659	1.3734
$Lf_{\beta_{1c}}$	1.0477	4.648	1.0743
$Z_{\delta_{col}}$	-22.3239	2.984	1.3503
$N_{\delta_{ped}}$	63.0040	3.876	1.8752
$N_{\delta_{col}}$	-32.4616	7.699	3.2056
$Mf_{\delta_{lat}}$	-0.0344	5.685	2.3049
$Mf_{\delta_{ion}}$	-0.2292	4.273	0.7825
$Lf_{\delta_{lat}}$	-0.2375	4.110	0.8904
$Lf_{\delta_{ion}}$	0.0286	18.377	6.3521
τ_f	0.0353	3.869	0.5679
$\tau_{\delta_{lat}}$	0.0369	1.980	0.6042
$\tau_{\delta_{ion}}$	0.0373	1.858	0.7552
$\tau_{\delta_{ped}}$	0.0456	2.279	1.1179
$\tau_{\delta_{col}}$	0.0398	2.665	1.3227

^atheoretical value

^bfixed in model

The design parameters of interest consisted of the stability margins, minimum disturbance rejection bandwidth (DRB), and the crossover frequency. Typical stability margins were used whereas the DRB and crossover frequencies were scaled using Froude laws from conventional helicopter values (Ref. 1). Table 7 presents the targeted design parameters for the roll axis.

Explicit model following was chosen as the control architecture for implementation as it is commonly employed in full scale vehicles and provides a flexible two degree of freedom design (Ref. 1). A block diagram of the EMF architecture for the roll axis is presented in Figure 9 and it is noted that the stability of the system is achieved by the feedback loop whereas the forward path provides the desired response characteristics. The EMF architecture is similar to dynamic inversion in that it employs an inverse plant; however, a significant advantage of the EMF architecture is that the inversion appears in the forward path. This distinct difference provides the advantage that model uncertainties do not jeopardize system stability making it a suitable candidate for small vehicles where modeling uncertainties are common.

Table 6. Roll Flap Stiffness Comparisons

Vehicle	N	$ L_{\beta_{fs}} $
R-50	1	588.9
Raptor 50	2.3	647.2
360CFX	3	5115
Honeybee	5	1273

Table 7. Roll Axis Control Design Goals

	Design
GM (dB)	6
PM (deg)	45
ω_c (rad/s)	11
ω_{DRB} (rad/s)	4
DRP dB	5

Design Tools

Simulink[®] Control Design and the MATLAB[®] Control System Toolboxes were utilized to tune the controller gains. These tools were sufficient for the simplistic design goals under consideration but do not provide the tailored needs necessary to arrive at an optimal design for a helicopter flight control system which requires a much larger set of design specifications (Ref. 1). The stability margins were imposed by the Margins TuningGoal noting that the toolbox evaluates the disk margins resulting in a more conservative design. The desired crossover frequency was imposed by setting the MinLoopGain and MaxLoopGain to values below and above the targeted crossover. Lastly, the DRB characteristics were imposed by the Rejection TuningGoal and the minimum attenuation profile depicted in Figure 10. The attenuation profile does not return to unity as one would expect and was done so in order to impose a constraint on the DRP without overly constraining the response. This is in contrast to typical rotorcraft flight control optimization that would explicitly optimize the -3 dB crossing and peak response.

Command Models

The command models in the EMF architecture prescribe the model performance exhibited by the vehicle. Second-order command models were utilized in the lateral and longitudinal axes whereas first order responses were used in the directional and heave axes. The roll command model employed a critically damped response with a natural frequency of 5 rad/s implemented in the form of Equation 23.

$$G_{cmd} = \frac{\omega_n^2}{s^2 + 2\zeta\omega_n s + \omega_n^2} \quad (23)$$

Inverse Plant and Equivalent Delay

The inverse plant provides the necessary feed-forward to promote good model following characteristics. In full scale rotorcraft it is common to utilize first order inverses; however, the

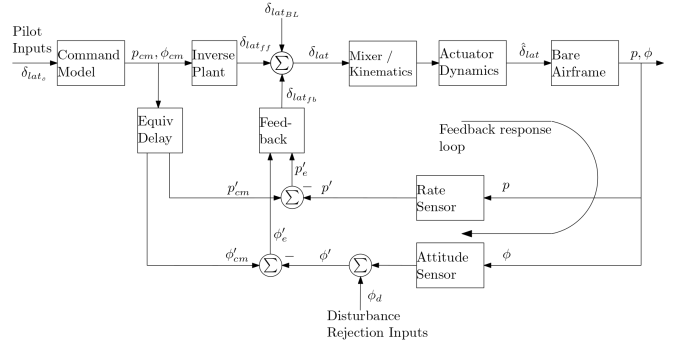


Figure 9. Explicit Model Following Roll Architecture

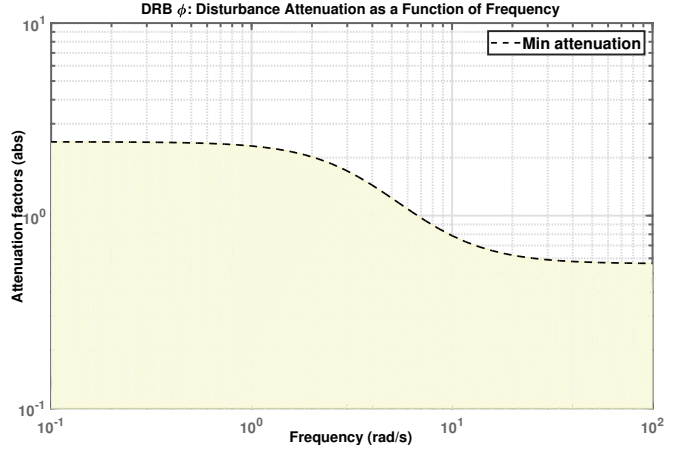


Figure 10. DRB Attenuation Profile

dominant second-order modes in the lateral and longitudinal axes require the use of a *second-order inverse*. This is in contrast to full-scale rotorcraft (and sub-scale multicopters) that generally use a lower-order (i.e. first order) inverse (Ref. 1). Mechanization of the second-order inverse requires a differentiating filter on the commanded rate output. Figure 11 presents the integrated command model and second-order inverse plant mechanization.

The second-order plant utilized in the inverse can be determined using the NAVFIT utility in CIPHER[®] to identify a low order model to the p/δ_{lat} response data. Another option that was utilized in this study is to extract the model using LINMOD from the Simulink design model with the other control loops closed using high gains. This approach is similar to the coupling numerator approach which provides the equivalent model subject to the other loops closed.

The equivalent delays synchronize the commands and measured rates thereby accounting for higher order dynamics that are not modeled. This synchronization helps prevent the actuators from being overdriven, but does not introduce a phase lag in the response to commanded inputs (Ref. 1). Numerical values for the delays are determined by breaking the loop and identifying a pure time delay to the phase delay between the aircraft response and the command signal as indicated by Equation 24. The two required responses were extracted from the Simulink model using LINMOD and the frequency re-

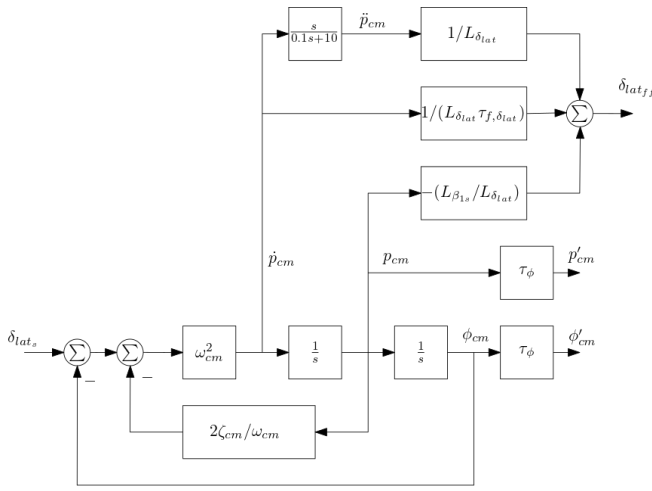


Figure 11. Lateral Integrated Command Model and Inverse Plant

response data was imported into CIFER[®] where the frequency response arithmetic utility was used to compute the response of interest before identifying the time delay using NAVFIT. The lateral axis equivalent delay was identified as 0.0371 sec.

$$\frac{p' / \delta_{lat_s}}{p_{cm} / \delta_{lat_s}} = e^{-\tau_{\phi} s} \quad (24)$$

Control Law Integration

A discrete formulation of the control laws was created in Simulink[®] and Simulink Coder was utilized to generate the CPP source code that could be integrated with ArduCopter. The ACAH control law was implemented by adding a new flight mode and interfaced with the INS rates and EKF attitude signals to be consistent with the identified model. This approach allowed the nominal control laws to remain intact while allowing the ACAH control law to be safely engaged once in an established hover. It should be noted that the ArduCopter architecture assumes the provided attitude controller is always utilized regardless of flight mode provided the majority of users do not alter the underlying control laws. This necessitated additional modifications that ensured the nominal attitude controller was not invoked when the ACAH controller was active thereby ensuring only one set of control outputs were sent to the servos. Automation of this process would be beneficial to facilitate the adoption of new ArduCopter versions without manually making modifications to override the underlying control laws.

SIL Validation Testing

The ArduCopter SIL environment was utilized to validate the discrete implementation of the control laws. The vehicle flight dynamics model was kept in the Simulink framework allowing the DERIVID model to be executed in the continuous time domain at a higher rate than the discrete control laws. The ArduCopter Autotest framework was utilized to run automated

scripts that could execute the required sweep tests and validation maneuvers.

Broken-loop sweeps for all axes were initially conducted and provided the necessary data to confirm the bare-airframe response (p / δ_{lat}) agreed with the original data. The necessary synchronization delays were determined by dividing the SIL response with the original data and identifying a time delay. During the broken-loop sweeps it was determined that the ArduCopter INS accelerometer and gyro filters were degrading the magnitude response in the SIL. To overcome this issue the filters were effectively disabled by setting their cutoff frequency to 200Hz from the default values of 20Hz utilized during flight testing. Figure 12 presents the observed response with the nominal 20Hz INS filter active and the improved agreement achieved by increasing the cutoff frequency. Note that the phase difference depicts an approximate 17 millisecond time delay which is similar to the kinematic inconsistency identified in the original flight data and is attributed to the INS filtering and signal reconstruction.

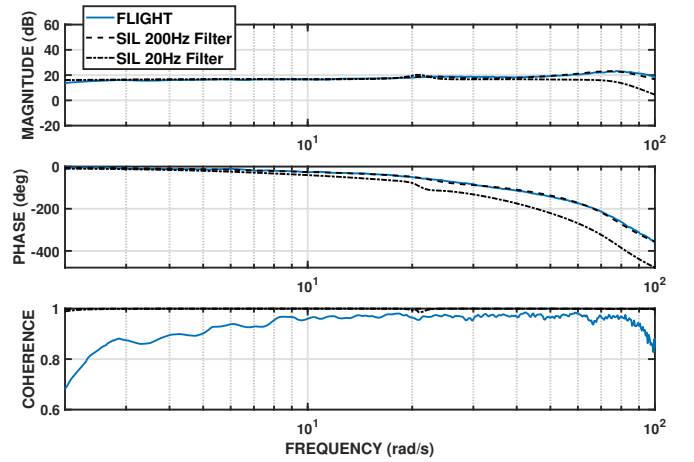


Figure 12. SIL Lateral Broken Loop Influence of INS Filters

The feedback control laws were validated in the SIL using a ground test sweep. The ground sweep was conducted by injecting the automated sweep in p' and the integral of the sweep in ϕ' thereby ensuring kinematically consistent inputs and is depicted in Figure 13. The result of the ground test $\delta_{lat_{fb}} / p'$, was compared to the Simulink LINMOD result from the design model and indicated excellent agreement as shown by the quadratic cost of 27.1 presented in Figure 14. Performing isolated feedback tests ensured the digital control laws were correctly implemented, an important step prior to conducting flight tests.

Further validation sweeps were conducted and compared against the Simulink design model including the broken-loop response ($\delta_{lat} / \delta_{lat_{BL}}$), disturbance rejection (ϕ' / ϕ_d), and the closed-loop response (ϕ / δ_{lat_s}). The SIL tests all provided excellent agreement and it was expected that the flight test would provide very similar results.

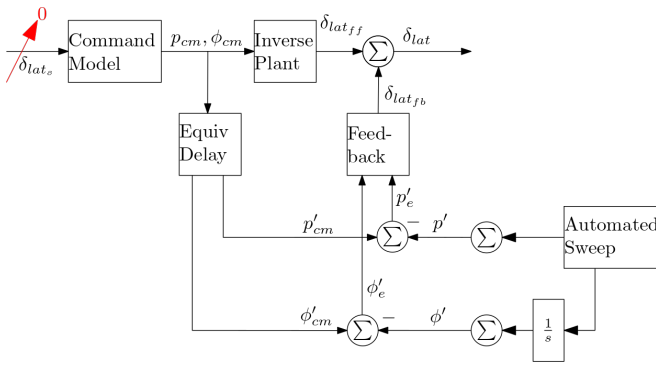


Figure 13. Lateral Feedback Sweep

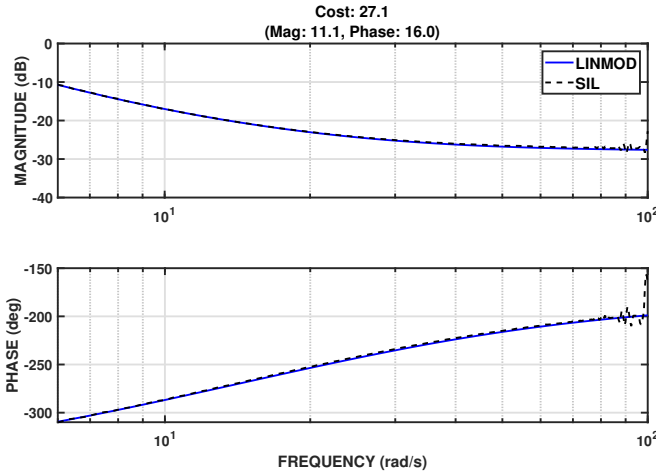


Figure 14. SIL Lateral Feedback Agreement with LINMOD

Flight Test Evaluation

The objective of the flight tests was to perform the final validation of the control system. Preliminary flights were utilized to fine tune the automated sweep amplitudes and ensure the new control system was well behaved under nominal flight conditions. Automated doublets were conducted as a preliminary check to ensure the controller was working as anticipated. Figure 15 demonstrates excellent tracking and minimal longitudinal excitation for a lateral doublet in flight.

Automated frequency sweeps for broken-loop, disturbance rejection, and closed-loop identification were conducted in all axes. Figure 16 compares the flight test broken-loop response to the design model and SIL responses. Throughout the frequency range of high coherence there is excellent agreement between the flight identified response and the design model.

The closed-loop response is presented in Figure 17 with the MUAD boundaries shaded for the desired model following response and demonstrates the flight response is within the acceptable boundaries. The lateral disturbance rejection is presented in Figure 18. The flight data exhibits acceptable agreement with the design model and it is noted the flight test sweep only extended to 40rad/s to avoid unnecessary shaking of the vehicle at high frequencies. Figure 18 also demon-

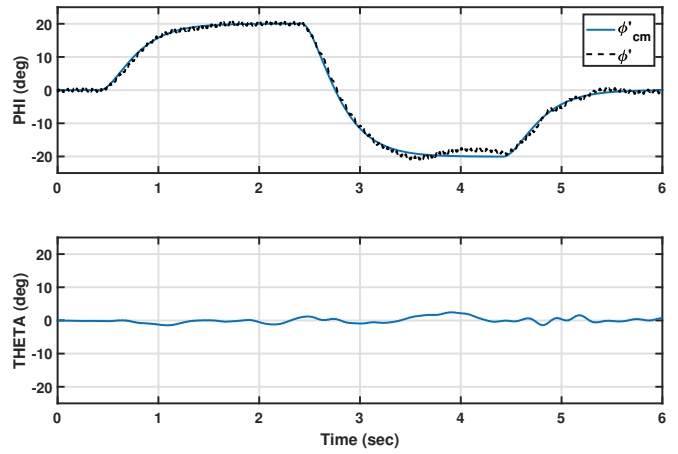


Figure 15. Flight Test Lateral Doublet

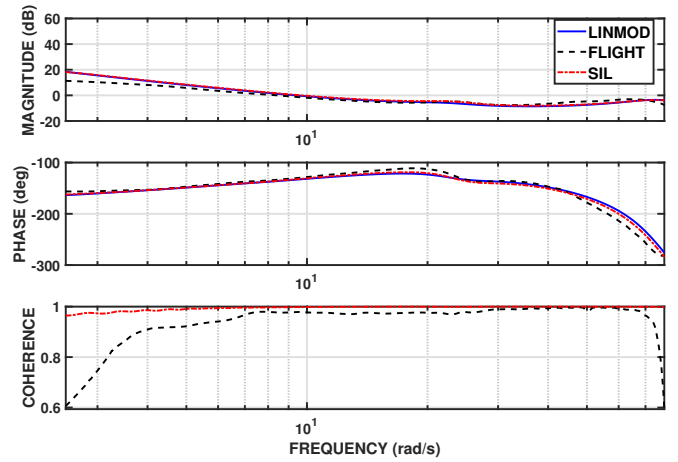


Figure 16. Lateral Control Broken-Loop Validation

strates the SIL provides excellent agreement with the design model throughout the broad frequency range. Note that the disturbance rejection doesn't decay to unity until after the lateral mode.

Table 8 presents the lateral controller specification comparison for the design model, SIL and flight test configurations. Overall, the controller performance is as designed with some loss in gain margin and crossover frequency. This discrepancy between the design and flight characteristics is most likely due the lack of sensor dynamics modeling in the Simulink design model.

CONCLUSIONS

This study used a methodical flight control development process typical of full-scale rotorcraft on a sub-scale flybarless 360CFX unmanned aerial system. Key elements of the development process were system identification of an accurate bare-airframe state-space model, an explicit model following flight control architecture, software-in-the-loop validation, and flight testing. The results of this study showed that:

1. System identification produced accurate bare-airframe

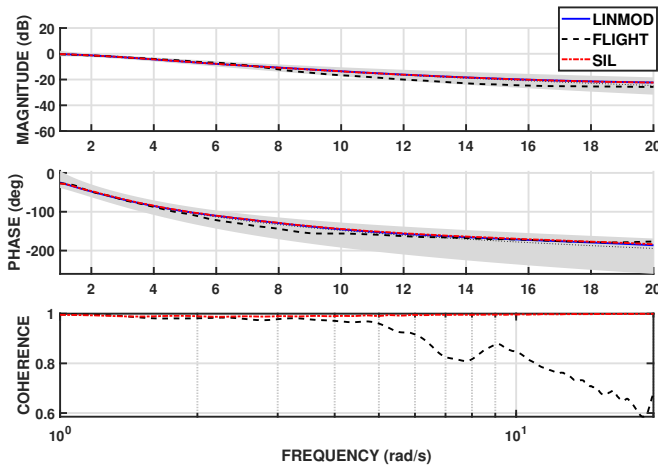


Figure 17. Lateral Control Closed-Loop Validation with MUAD Boundaries

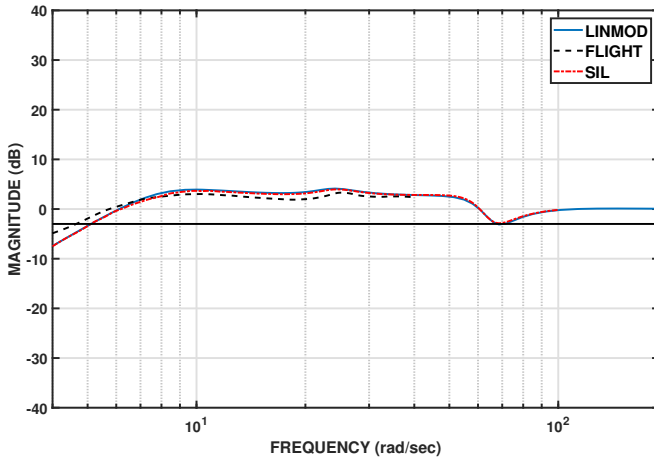


Figure 18. Lateral Control DRB Validation

frequency response data for the 360CFX flybarless sub-scale helicopter, based on automated flight-test frequency sweeps conducted with the legacy control system engaged, and the Pixhawk (CUAVv5) sensor suite. Synchronization corrections were required to align the attitude and angular rate signals as a result of onboard filtering applied to the INS angular rates and accelerations.

2. The 360CFX sub-scale conventional helicopter configuration exhibits strong rotor-fuselage pitch and roll coupling, thus requiring the hybrid model structure which has an explicit model of the rotor flapping dynamics. The directional and heave dynamics were adequately modeled using the quasi-steady model. The absence of a flybar results in coupled rotor/fuselage dynamics that are much higher in frequency and a much shorter effective response time constant than flybar equipped vehicles.
3. An explicit model following (EMF) control system architecture, commonly used for fly-by-wire full-scale rotorcraft, is well suited to small-scale single main rotor

Table 8. ACAH Lateral Control Law Design Specification Comparison with Flight Data

	Design	SIL	Flight
GM (dB)	7.1	6.5	4.7
PM (deg)	48.7	48.2	46.4
ω_c (rad/s)	9.3	9.7	8.4
ω_{DRB} (rad/s)	5.1	5.1	4.65
DRP (dB)	4.7	4.0	3.3
ω_{BW} (rad/s)	11.1	11.7	12.6
τ_p (s)	0.0378	0.0338	0.0346

helicopter unmanned air systems. Due to the strong rotor-fuselage coupling a second-order inverse is needed. The mechanization of the second-order inverse requires a causal differentiator. Control gains were tuned using MATLAB® to provide a targeted crossover frequency, adequate stability margins, and a targeted disturbance rejection bandwidth.

4. Software-in-the-loop (SIL) testing was a valuable tool to demonstrate the digital control laws were correct. The INS filters produced a different response than that observed during flight and may warrant further investigation.
5. The vehicle flew well during flight testing and in general there was good agreement between the flight test data and the Simulink design model, thereby validating the methodical flight control development process that is typical of full-scale rotorcraft.

Author contact:

Jeffrey Walker jwalker@bihrl.com

Mark B. Tischler mrtischler@aol.com

REFERENCES

1. Tischler, M. B., Cheung, K. K., and Soong, J. Y., *Practical Methods for Aircraft and Rotorcraft Flight Control Design: An Optimization-Based Approach*, AIAA Education Series, AIAA, Reston, VA, April 2017.
2. Tischler, M. B., and Remple, R. K., *Aircraft and Rotorcraft System Identification Engineering Methods with Flight Test Examples*, AIAA Education Series, AIAA, Reston, VA, second edition, November 2012.
3. Cheung, K. K., Wagster, J. A., Tischler, M. B., Ivler, C. M., Berrios, M. G., Berger, T., Lehmann, R. M., Juhasz, O., Tobias, E. L., Goerzen, C. L., Barone, P. S., Sanders, F. C., and Lopez, M. J. S., "An Overview of the U.S. Army Aviation Development Directorate Quadrotor Guidance, Navigation, and Control Project," American Helicopter Society 73rd Annual Forum & Technology Display, Fort Worth, Texas, 2017.
4. Mettler, B., *Identification Modeling and Characteristics of Miniature Rotorcraft*, Kluwer Academic Publishers, Norwell, MA, 2010.

5. Bhandari, S., and Colgren, R., "A High-Order Flight Dynamics Model for Raptor 50 UAV Helicopter Using CIFER," American Helicopter Society International Specialists' Meeting on Unmanned Rotorcraft, 2007.
6. Gong, A., Sanders, F. C., Hess, R. A., and Tischler, M. B., "System Identification and Full Flight-Envelope Model Stitching of a Package-Delivery Octocopter," AIAA SciTech 2019 Forum, San Diego, California, 2019. DOI: 10.2514/6.2019-1076
7. Alvarenga, J., Vitzilaios, N. I., Rutherford, M. J., and Valavanis, K. P., "Modeling and Frequency-Domain Parameter Identification of a Small-Scale Flybarless Unmanned Helicopter," *Encyclopedia of Aerospace Engineering*, John Wiley & Sons, Ltd., 2016, pp. 1–27. DOI: 10.1002/9780470686652.eae1155
8. Alvarenga, J., Vitzilaios, N. I., Rutherford, M. J., and Valavanis, K. P., "Scaled Control Performance Benchmarks and Maneuvers for Small-Scale Unmanned Helicopters," 54th IEEE Conference on Decision and Control (CDC), Osaka, Japan, 2015.
9. Gardner, R. C., Humbert, J. S., and Chopra, I., "Maneuverability Comparison of Flybar and Flybarless Micro-Helicopters," American Helicopter Society 5th Unmanned Rotorcraft and Network Centric Operations, Scottsdale, AZ, 2013.
10. Taamallah, S., "Small-Scale Helicopter Blade Flap-Lag Equations of Motion for a Flybarless Pitch-Lag-Flap Main Rotor," AIAA Modeling and Simulation Technologies Conference, Portland, Oregon, August 2011. DOI: 10.2514/6.2011-6279
11. Taamallah, S., "A Flight Dynamics Model for a Small-Scale Flybarless Helicopter," Technical Report NLR-TP-2016-025, NLR, Netherlands, 2016.
12. Zhou, B., Lu, X., Tang, S., and Zheng, Z., "Nonlinear System Identification and Trajectory Tracking Control for a Flybarless Unmanned Helicopter: Theory and Experiment," *Nonlinear Dynamics*, Vol. 96, (4), June 2019, pp. 2307–2326. DOI: 10.1007/s11071-019-04923-9
13. Lorenzetti, J. S., Bañuelos, L., Clarke, R., Murillo, O. J., and Bowers, A., "Determining Products of Inertia for Small Scale UAVs," 55th AIAA Aerospace Sciences Meeting, Grapevine, Texas, January 2017. DOI: 10.2514/6.2017-0547
14. Jardin, M., and Mueller, E., "Optimized Measurements of UAV Mass Moment of Inertia with a Bifilar Pendulum," AIAA Guidance, Navigation and Control Conference and Exhibit, Hilton Head, South Carolina, August 2007. DOI: 10.2514/6.2007-6822
15. "ArduPilot," <https://www.ardupilot.org>.
16. Geyer, B., "ArduPilot v3.6," https://github.com/bnsgeyer/ardupilot/tree/Copter-3.6_freq_sweep.
17. Papaliakos, G., "ArduPillog," <https://github.com/Georacer/ardupillog>.
18. Conroy, J. K., Humbert, J. S., and Pines, D. J., "System Identification of a Rotary-Wing Micro Air Vehicle," *Journal of the American Helicopter Society*, Vol. 56, (2), April 2011, pp. 25001–250014. DOI: 10.4050/JAHS.56.025001